SCIENTIFIC REPORTS
nature research

Check for updates

OPEN

Enhancement of photovoltage by electronic structure evolution in multiferroic Mn-doped $BiFeO_3$ thin films

Seiji Nakashima[1]✉, Tohru Higuchi[2], Akira Yasui[3], Toyohiko Kinoshita[3], Masaru Shimizu[1] & Hironori Fujisawa[1]

The bulk photovoltaic effect (BPVE) is a mechanism of recent focus for novel solar cells that exceed the power conversion efficiency of p–n junction solar cells because of the quantum mechanical effect to generate photocurrent known as shift current. Ferroelectrics are receiving attention again because of their high voltage generation by the BPVE and converse piezoelectric effect to realize high performance optical actuators. We have investigated the BPVE in ferroelectric $BiFeO_3$ (BFO) single crystal thin films, whereby the photovoltage was enhanced by Mn doping, and 852 V generation was demonstrated at 80 K. The enhancement mechanism was also investigated using soft and hard X-ray photoelectron spectroscopy (SXPES, HAXPES), and soft X-ray absorption spectroscopy with synchrotron radiation. This report reveals a way to new voltage source applications employing the BPVE for high impedance devices with ferroelectrics. Important aspects for designing ferroelectric materials by impurity doping are also discussed.

The bulk photovoltaic effect (BPVE)[1–5] in ferroelectric materials has been intensively investigated because of properties such as above bandgap photovoltage generation or the possibility of high power conversion efficiency that exceeds the Shockley–Queisser limit[6]. One of the most highly anticipated applications that could take advantage of such high photovoltage is optical actuators using ferroelectrics that exhibit inverse piezoelectric properties[7–9]. The electric field generated by the BPVE in ferroelectrics is caused by strain due to the converse piezoelectric effect; therefore, optical strain could be induced by the coupling of these effects.

Optically induced strain in ferroelectrics has been previously investigated for $BaTiO_3$[9] and (Pb,La)(Zr,Ti)O_3 (PLZT)[7,8]; however, some issues remain to be overcome. Firstly, the mechanism of the BPVE has not yet been completely clarified, although the piezoelectricity in ferroelectrics has been intensively investigated since the discovery of a morphotropic phase boundary (MPB) in Pb(Zr,Ti)O_3 (PZT). Secondly, typical ferroelectrics such as $BaTiO_3$ and PZT have a bandgap in the UV light region of > 3 eV[10,11], making the desired visible light utilization difficult.

Regarding the first issue, a shift current has recently been discussed intensively as one of the mechanisms for the BPVE[12–17]. The shift current is a quantum mechanical effect that generates photocurrent, which has quite a different mechanism from that of p–n junction type solar cells. With respect to the photocurrent generated by the shift current, although it is responsive to unpolarized light, an even larger response is expected under polarized light. The ferroelectric polarization is also closely related to the shift current response, although it is not necessary for the generation of a shift current. A larger open circuit voltage (V_{OC}) can also be obtained in a highly insulating medium.

Regarding the second issue, $BiFeO_3$ (BFO) is an environmental-friendly, lead-free multiferroic that simultaneously exhibits excellent ferroelectric properties and antiferromagnetism[18,19]. The bandgap of BFO is in the visible wavelength region of 2.5–2.8 eV[20,21], by which visible light driven devices can be realized. In addition, super-long-time relaxation of photo-induced influence have also reported[22]. Ultra-fast response and optical

[1]Department of Electronics and Computer Science, Graduate School of Engineering, University of Hyogo, Himeji, Hyogo 671-2201, Japan. [2]Department of Applied Physics, Tokyo University of Science, Katsushika, Tokyo 125-8585, Japan. [3]Japan Synchrotron Radiation Research Institute / SPring-8, Sayo, Hyogo 679-5198, Japan. ✉email: nakashima@eng.u-hyogo.ac.jp

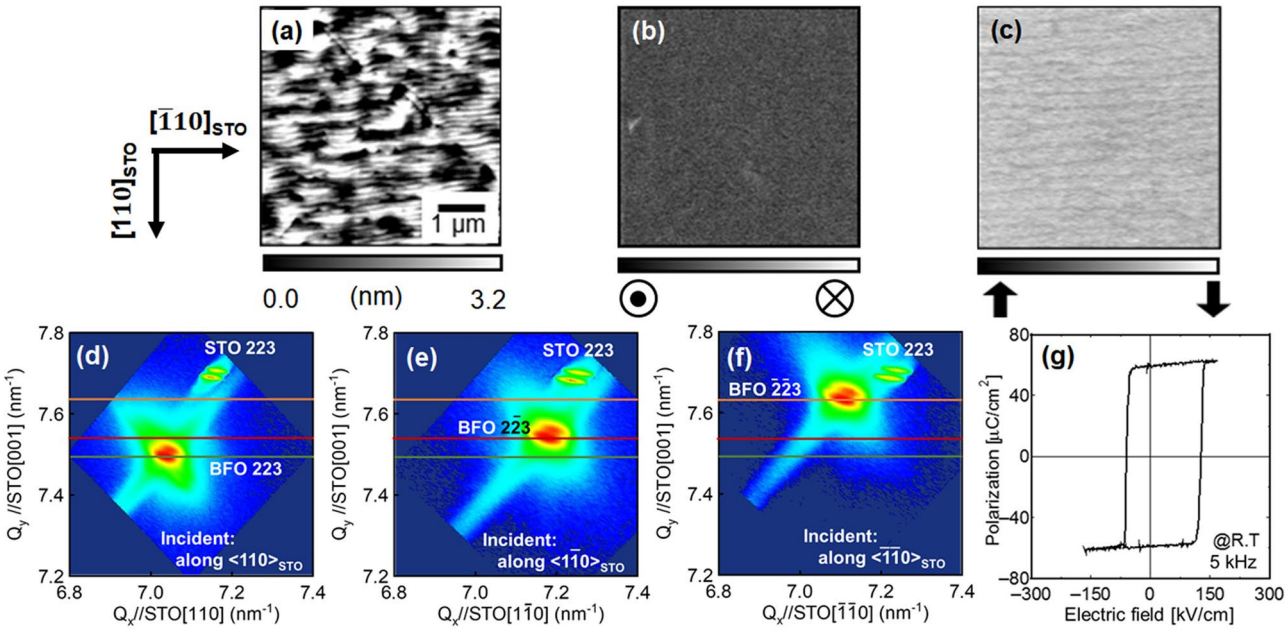

Figure 1. **a** Surface AFM image of 1 μm thick Mn 1 at%-doped BFO thin film grown on SRO-buffered STO, and **b** vertical- and **c** lateral-PFM images of the thin film. XRD-RSM around **d** BFMO 223, **e** BFMO 22$\bar{3}$, and **f** BFMO $\bar{2}\bar{2}$3 diffraction spots. **g** Dielectric displacement–electric field hysteresis loop of the thin film measured at RT. Note that the BFMO thin film is a single crystal and shows an excellent ferroelectric *D*–*E* hysteresis loop.

strain[23] with its modulation by magnetic fields[24] have already been reported for multiferroic BFO. However, the strain in BFO thin films can only be observed under irradiation by a femtosecond laser. Even bulk BFO single crystals show only a small strain of ca. 0.0002%. To enhance the optical strain, enhancement of the photovoltage is required; therefore, a highly insulating BFO thin film is necessary.

Here, we demonstrate a photovoltage above 852 V due to the BPVE in a lead-free multiferroic Mn-doped $BiFeO_3$ (BFMO) single crystal thin film. We also clarify that evolution of the electronic structure by the Mn-doping of BFO has an important role in enhancement of the photovoltage.

Results

BFMO thin film growth. To characterize the BPVE of BFMO thin films, a single crystal film is suitable because the geometric relation between the incident light polarization and the BFMO crystal has a strong effect on the photocurrent. In addition, the BPVE measurements were performed in the film plane, meaning that film orientation having lower azimuthal angle $\boldsymbol{P}_s$ vector is suitable. Therefore, 1 μm thick BFMO thin films with various amounts of dopant (0, 0.5, 1.0, 3.0 and 10 at%) were grown on vicinal $SrTiO_3$(001) (STO) substrates by conventional RF planar magnetron sputtering process. Vicinal STO substrates with the $[001]_{STO}$ direction inclined 4° toward $[110]_{STO}$ have been used for the domain engineering[25–28] of BFMO thin films. Figure 1a–c show surface atomic force microscopy (AFM), and vertical and lateral piezoresponse force microscopy (PFM) images of a Mn 1 at%-doped BFO thin film. The BFMO thin film has a well-aligned step-and terrace structure with the step propagation direction along $[110]_{STO}$, which indicates step-flow growth of the film. The vertical and lateral PFM images show uniform contrast, which reveals that the spontaneous polarization ($\boldsymbol{P}_s$) direction is aligned along the $[111]_{STO}$ direction over the entire region.

For macroscopic characterization, X-ray diffraction reciprocal space mappings (XRD-RSMs) around BFO 223, $\bar{2}23/2\bar{2}3$ and $\bar{2}\bar{2}3$ diffraction spots were measured, as shown in Fig. 1d–f, respectively. All mappings show a single BFMO diffraction spot, except for the diffraction spots from the STO substrate. The doubled spots in each pattern are due to the mixed incidence of Cu $K\alpha_1$ and $K\alpha_2$ radiation. These BFMO {223} spots have three different d-spacings due to the rhombohedral symmetry. Furthermore, microscopic and macroscopic structural analyses reveal that the BFMO film is completely single crystal, and that 0, 0.5, and 3.0 at% Mn-doped BFMO thin films are also single crystal. Details of the domain structure of the BFMO thin films are described in the Supplementary Information.

To confirm the ferroelectricity of the BFMO thin films, ferroelectric *D-E* hysteresis loops of Pt/1 μm thick BFMO/$SrRuO_3$ (SRO)/STO capacitor structures were measured. The capacitor with a 1 at% Mn-doped BFMO thin film shows well-saturated square shape *D-E* hysteresis loops at room temperature (RT), as shown in Fig. 1g. The double remanent polarization ($2P_r$) and double coercive field ($2E_C$) of the BFMO thin film were 120 μC/cm^2 and 250 kV/cm, respectively. The $2P_r$ value agrees well with that for BFO bulk single crystal[20]. The other samples, except for the 10 at% Mn-doped BFMO thin film, also showed well-saturated square shape *D-E* hysteresis loops at RT (see Supplementary Information).

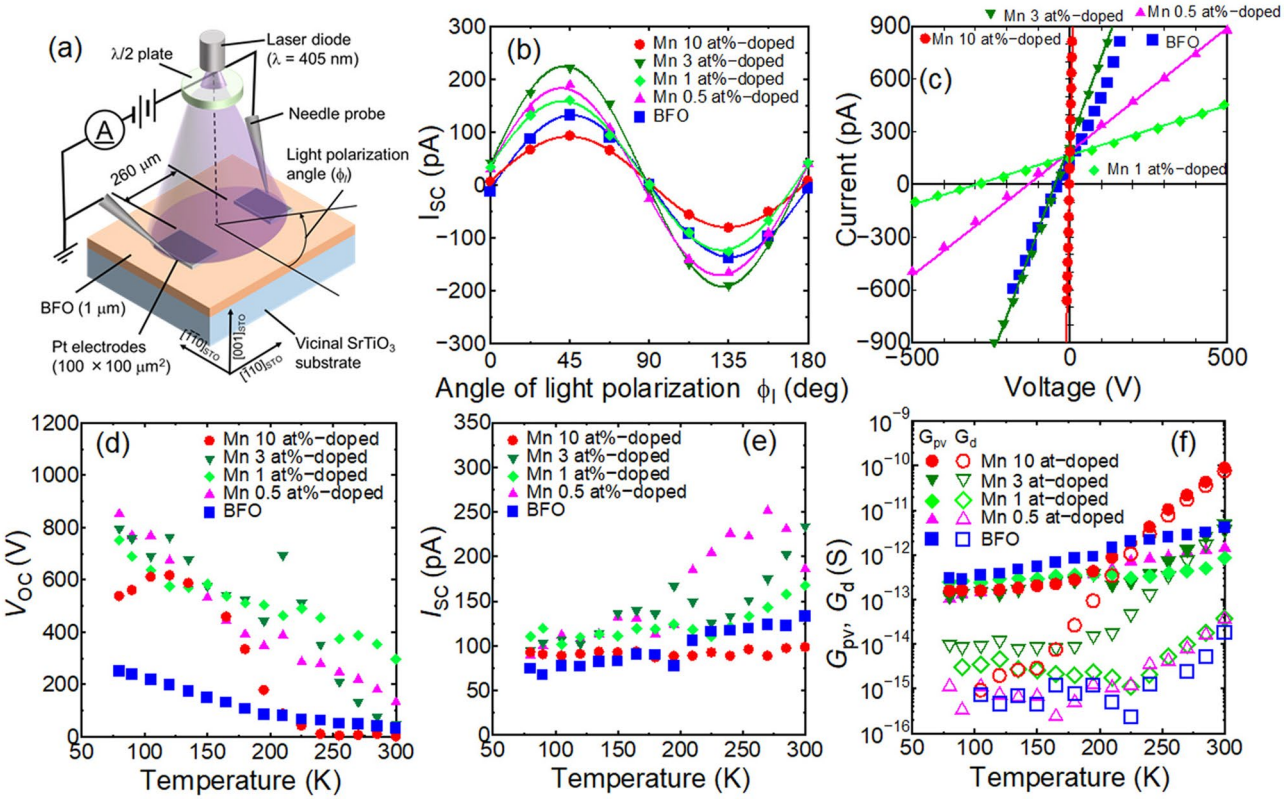

Figure 2. **a** Schematic illustration of the setup for photovoltaic property measurements. **b** Dependence of the light polarization angle on the short circuit current (I_{SC}). **c** *I*–*V* characteristics, and temperature dependence of **d** I_{SC}, **e** open circuit voltage (V_{OC}), **f** photoconductance (G_{pv}) and dark conductance (G_d) for BFMO thin films with various amounts of Mn doping. The photovoltaic properties were measured under irradiation from a blue violet laser (λ = 405 nm). The light polarization angle (ϕ_l) was fixed at 45° in **c**–**f**. Note that the maximum V_{OC} was 280 V at RT for Mn 1 at%-doped BFO, and was 852 V at 80 K in Mn-0.5 at%-doped BFO thin films.

BPVE in BFMO thin films. To characterize the BFMO thin films, Pt/BFMO/Pt coplanar capacitors were fabricated on vicinal STO substrates, as shown in Fig. 2a. Pt electrodes (100 × 100 μm²) were fabricated on the BFMO surface along the $[1\bar{1}0]_{STO}$ direction with an inter-electrode distance of 260 μm. The current–voltage (*I*–*V*) characteristics of the Pt/BFMO/Pt coplanar capacitors were measured at RT under irradiation from a blue violet laser (λ = 405 nm). For these measurements, light polarization was always kept in the film plane and the laser power density was set at 17 W/cm² using a 60 mW laser diode.

Figure 2b shows the dependence of the light polarization angle (ϕ_l) on the short circuit current (I_{SC}) of the Pt/BFMO/Pt coplanar capacitors. Light polarization along the $[100]_{STO}$ direction is represented by $\phi_l = 0°$. The light polarization was then rotated by inserting a λ/2 plate. A positive ϕ_l indicates counterclockwise rotation of the light polarization. The I_{SC} values for the Pt/BFMO/Pt capacitors with various amounts of Mn dopant in the BFMO layer showed doubling sinusoidal changes, which indicates that the photocurrents are due to the BPVE.

In principle, the BPVE is a second-order nonlinear optical effect that includes carrier excitation processes. Therefore, the photocurrent $\boldsymbol{J}_i$, can be given as

$$\boldsymbol{J}_i = I_0 \boldsymbol{\beta}_{ijk} \boldsymbol{e}_j \boldsymbol{e}_k, \tag{1}$$

where I_0 is the incident light intensity, $\boldsymbol{\beta}_{ijk}$ is the bulk photovoltaic tensor of rank three, and $\boldsymbol{e}_j$ and $\boldsymbol{e}_k$ are components of the light polarization vectors of two photons. For BFO crystals belonging to the point group 3 m, Eq. 1 can be represented by

$$\begin{pmatrix} j_1 \\ j_2 \\ j_3 \end{pmatrix} = I_0 \begin{pmatrix} 0 & 0 & 0 & 0 & \beta_{15} & -\beta_{22} \\ -\beta_{22} & \beta_{22} & 0 & \beta_{15} & 0 & 0 \\ \beta_{31} & \beta_{31} & \beta_{33} & 0 & 0 & 0 \end{pmatrix} \begin{pmatrix} e_1^2 \\ e_2^2 \\ e_3^2 \\ e_2 e_3 \\ e_3 e_1 \\ e_1 e_2 \end{pmatrix}. \tag{2}$$

where the first index of the tensor components corresponds to the current direction and the second index is that used in Voigt reduced notation. The coordinates of the system are Cartesian coordinates $\{\boldsymbol{x}_i\}$ with

$\boldsymbol{x}_1 = \left(\frac{a}{2}, -\frac{a}{2\sqrt{3}}, \frac{c}{3}\right)$, $\boldsymbol{x}_2 = \left(0, \frac{a}{\sqrt{3}}, \frac{c}{3}\right)$, and , $\boldsymbol{x}_3 = \left(-\frac{a}{2}, -\frac{a}{2\sqrt{3}}, \frac{c}{3}\right)$, where a and c are the lattice constants of BFO with a hexagonal setting. From Eqs. 1 and 2, I_{SC} of the Pt/BFMO/Pt coplanar capacitor can be given by

$$I_{SC} \propto I_0(-0.41\beta_{15} - 0.574\beta_{22}) \sin 2\phi_l. \tag{3}$$

This theoretical formula agrees well with the experimental results given in Fig. 2b. The maximum I_{SC} was determined to be $\phi_l = 45°$, which is in good agreement with that for the BPVE in BFO-based materials[29–33].

The enhancement of I_{SC} by Mn-doping of BFO was also confirmed. A maximum I_{SC} of 224 pA was confirmed for the Mn 3 at%-doped BFO thin film, which is known as gap-state engineering, as proposed by Matsuo et al.[34] However, the lower I_{SC} for the Mn 10 at%-doped BFO thinilm indicated an increase in free carriers that absorb incident light.

Mn doping was determined to significantly change the I–V characteristics of the Pt/BFMO/Pt coplanar capacitors under light irradiation. From Fig. 2c, the V_{OC} increased significantly up to a Mn doping amount of 1 at%, and the maximum value reached 280 V, which corresponds to an electric field of 10.8 kV/cm. For doping over 1 at% Mn, V_{OC} decreased significantly. Theoretically, V_{OC} can be expressed by

$$V_{OC} = \frac{I_{SC}d}{G_d + G_{pv}}, \tag{4}$$

where d is the inter-electrode distance, and G_d and G_{pv} are the conductance under dark and irradiation conditions, respectively. Equation 4 reveals that V_{OC} was enhanced by a decrease in the conductivity or an increase in I_{SC}. According to the I-V characteristics shown in Fig. 2c, although I_{SC} did not change significantly, the conductance did vary significantly due to Mn-doping. Therefore, the enhancement of V_{OC} is due to a decrease of the photoconductance in the BFMO thin films.

Notably, V_{OC} was significantly enhanced at low temperature. In particular, V_{OC} for Mn-doped BFO was significantly increased, as shown in Fig. 2d. A maximum V_{OC} of 852 V was obtained for Mn 0.5 at%-doped BFO at 80 K, which corresponds to an electric field of 32.8 kV/cm. Details of the photovoltaic properties at 80 K are described in the Supplementary Information. The drastic enhancement of V_{OC} was also due to the decrease of conductance under dark and irradiation conditions. I_{SC} as shown in Fig. 2e was not so significantly increased; however, the dark- and photoconductance were significantly decreased with the temperature, as shown in Fig. 2f. As a result, the enhancement of V_{OC} in Mn-doped BFO thin films is considered to be caused by an enhancement of the insulation properties. Since the discovery of ferroelectricity in BFO thin films, Mn doping of BFO has been intensively investigated to decrease the leakage current of BFO thin films; however, the influence of Mn doping on the electronic structure remains unclear.

Electronic structure of Mn-doped BFO thin films. To clarify the influence of Mn-doping in BFO on the electronic structure, soft X-ray photoemission spectroscopy (SXPES) and soft X-ray absorption spectroscopy (SXAS) using synchrotron radiation was performed on 0.5 and 3 at% Mn-doped BFO thin films at RT. 150 nm thick single crystal BFMO thin films were fabricated on $SrRuO_3$-buffered vicinal STO(001) single crystal substrates. For preventing from charging up during SXPES and SXAS spectra, the maximum thickness is 150 nm. According to our previous study[28], epitaxial strains of 150 nm and 1 μm thick BFO thin films can be estimated as -0.45% and − 0.30%, respectively, indicating small difference. In addition, the first principles calculations predicted that the epitaxial strains mainly cause symmetrical change of the electronic structure[36]. Moreover, it has already proved experimentally that the BFO thin films with various film thickness show constant bandgap[37]. Therefore, influence of the Mn doping on the valence band and conduction band spectra of the BFO thin films can be evaluated by using 150 nm thick films. Figure 3a shows the valence and conduction band spectra of the BFMO thin films. The 3 at% Mn-doped BFO thin film has a slightly smaller bandgap (E_g) of ca. 2.0 eV compared to that of the 0.5 at% Mn-doped BFO at ca. 2.3 eV. However, a broad density of states (DOS) was observed above the valence band in the 0.5 at% Mn-doped BFO thin film, which caused a Fermi level shift of ca. 1.1 eV. O 1 s Fe 2p SXPES spectra also shifted by ca. 1.1 eV due to the Mn-doping of BFO (see Supplementary Information).

SXPES is a very powerful method for the investigation of the electronic structure of a material surface; however, characterization of a ferroelectric surface is very difficult due to polarization charges. Spontaneous polarization charges at the surface of a ferroelectric are generally terminated by molecules adsorbed from the air. However, the surface potential is unstable because of its floating potential. Therefore, the surface potential of the ferroelectrics in an ultrahigh vacuum should be more unstable due to unstable termination of the spontaneous polarization charges. Therefore, the SXPES and SXAS spectral shift with ferroelectrics cannot be completely elucidated.

Hard X-ray photoemission spectroscopy (HAXPES) of ultrathin metal film-capped surfaces is suitable for the precise evaluation of Fermi level shifts in ferroelectrics. The ferroelectric polarization charge is terminated by ultrathin metal films, which indicates that the Fermi level of the ferroelectric at the metal/ferroelectrics interface is pinned by that of the metal. HAXPES can also be used to evaluate a ferroelectric layer through the capped ultrathin metal film due to the deep penetration depth (> 20 nm) of high energy photoelectron.

Figures 3b,c show Au 4f and Bi 4f HAXPES spectra, respectively, for the Au (9 nm) capped Mn 1 at%-doped BFO/SRO/STO structure measured using 8 keV synchrotron X-rays with take-off angles (TOAs) of 85° (TOA85) and 5° (TOA5). The low and high TOAs mean surface and bulk sensitive conditions, respectively. The Bi 4f spectra with a TOA of 5° is slightly shifted to lower binding energy compared to those with TOA of 85°, which reveals that the energy bands of BFMO were bent up near the Au/BFMO interface. Figure 3d shows a larger shift of the Bi 4f spectra with an increase in the amount of Mn doping. The difference between the binding energy of Bi 4f spectra with TOAs of 85° and 5° also increased clearly with the amount of Mn doping. With an almost constant

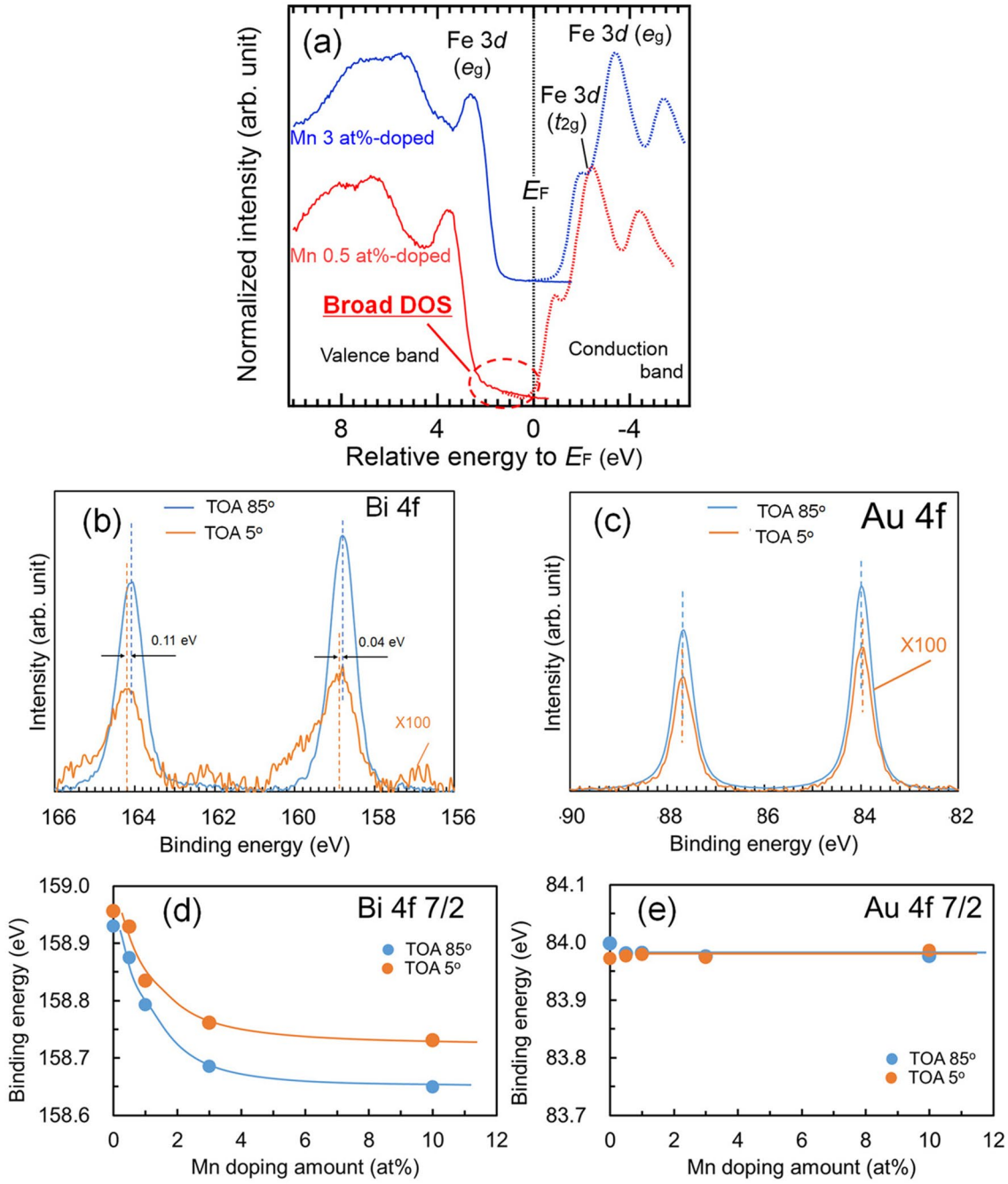

Figure 3. **a** Valence and conduction band spectra for Mn 0.5 at%-doped (blue line) and 3 (red line) at%-doped BFO thin films measured using SXPES and SXAS, HAXPES spectra of **b** Bi 4f and **c** Au 4f orbitals measured at TOAs of 5° (orange line) and 85° (blue line). Dependence of **d** Bi $4f_{7/2}$ and **e** Au $4f_{7/2}$ binding energies measured at TOA of 5° (orange line) and 85° (blue line) on the amount of Mn doping. The broad DOS above the valence band is denoted by a red-dashed line in **a** and was observed in the Mn 0.5 at%-doped BFO thin film but vanished in the Mn-3 at%-doped BFO thin film.

binding energy of the Au 4f spectra, as shown in Fig. 3e, the Fermi level in the BFMO decreased with an increase in the amount of Mn doping.

Discussion

From Fig. 2, V_{OC} above the bandgap is due to the BPVE. Bhatnagar et al.[35] already reported an above-bandgap V_{OC} of ca. 55 V at 80 K due to the BPVE and domain wall photovoltaic effect. The V_{OC} corresponds to an electric field of 5.5 kV/cm. On the other hand, V_{OC} in non-doped BFO at 80 K in the present study was 251 V, which corresponds to an electric field of 9.7 kV/cm. When the difference of film thickness between the present study and the previous study is considered, the V_{OC} of non-doped BFO in Fig. 2 was in agreement with that in the previous study. In contrast, the V_{OC} of 852 V for Mn 0.5 at%-doped BFO indicates a significant enhancement. According

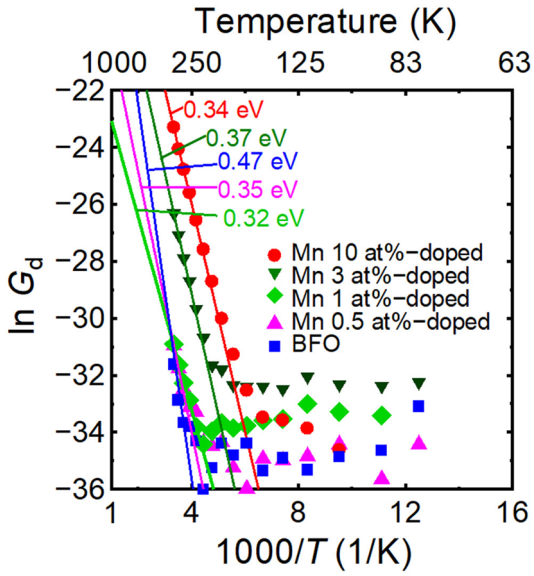

Figure 4. Arrhenius plot of dark conductance (G_d) for BFMO thin films with various amounts of Mn doping. The values in the figure denote the slopes of the lines, which indicate activation energies. Note that the significant increase of G_d near RT in Mn-doped BFO is due to traps with a depth around 0.35 eV.

to Eq. (4), V_{OC} is a function of I_{SC}, G_d and G_{pv}. However, I_{SC} did not change significantly by Mn doping or by variation of the temperature when compared to the V_{OC} enhancement shown in Fig. 2c. The low temperature dependence of I_{SC} is an important feature of the BPVE, which indicates that I_{SC} is independent of the carrier mobility. In addition, G_{pv} was sufficiently larger than G_d, as shown in Fig. 2f; therefore, the enhancement of V_{OC} was mainly caused by the decrease of G_{pv}.

An improvement of insulation by the Mn doping of BFO has been investigated by many researchers[38–40], although the mechanism of this improvement remains unclear. However, Noguchi et al.[41] recently predicted by first principles calculations that trapping oxygen vacancies at the nearest O site of a doped Mn atom causes the impurity state above the valence band to disappear, which indicates an improvement of the insulation of Mn-doped BFO. A broad DOS is clearly evident in Mn 0.5 at%-doped BFO, as indicated by the red-dashed circle in Fig. 3a. In contrast, the broad DOS vanishes in Mn 3 at%-doped BFO. These results are in good agreement with the prediction reported by Noguchi et al.[39], which indicates that these results experimentally confirm that oxygen vacancies trapped around doped-Mn atoms improve the insulation of Mn-doped BFO.

In addition, Fig. 3 shows that the Mn doping of BFO is acceptor doping, which indicates the introduction of impurity states. To evaluate these impurity states, G_d shown in Fig. 2e was replotted on an Arrhenius plot, as shown in Fig. 4. The slopes in Fig. 4 indicate the activation energy of the excited carriers. The activation energy can be evaluated to be ca. 0.35 eV in the BFMO thin films, despite a larger activation energy in non-doped BFO thin film. Therefore, the Fermi level shift as shown in Fig. 3 is due to these impurity states. Matsuo et al.[34] have already reported that Mn doping of BFO creates half-occupied states ca. 1 eV from the valence band edge, from first principles calculations, considering a Mn valence of 3 + . This impurity state is slightly different from our experimental result of 0.35 eV. However, assuming a Mn impurity state that is 0.35 eV from valence band edge, the half-occupied state is filled by thermally excited electrons, as shown in the Arrhenius plot of Fig. 4; therefore, the Mn valence should be 2 + at RT and Mn doping could act as acceptor doping.

In conclusion, Mn-doping of BFO enhanced the photovoltage induced by the BPVE. In a Pt/Mn 1 at%-doped BFO/Pt coplanar capacitor with an inter-electrode distance of 260 μm, V_{OC} reached 280 V at RT (852 V at 80 K). This enhancement is considered to be due to improvement of the insulation of BFMO. Mn doping of BFO causes lowering of the Fermi level; however, the improvement of insulation was due to the disappearance of impurity states above the bandgap, which is an oxygen vacancy trapping effect around Mn dopant atoms. The high voltage generation realizes the application of a high electric field in the BFMO thin film itself. Thus, we have discovered a new voltage source application for high impedance devices using ferroelectrics. Moreover, we presented experimental evidence for the influence of impurity doping of ferroelectrics on the electronic structure and electrical properties. These results provide important aspects for control of the conductivity of ferroelectrics by impurity doping.

Methods

Sample preparation. Vicinal STO(001) single crystals were used as substrates for all samples. A Ti–O terminated surface was formed by wet etching with buffered-HF solution and annealing at 1,000 °C for 1 h in the atmosphere. For samples for SXPES, SXAS, and HAXPES measurements, 30 nm thick SRO thin film was epitaxially grown on the vicinal STO surface by an RF planar magnetron sputtering process. For SRO thin film growth, a 2 inch diameter SRO ceramic was used as a target. The substrate temperature, sputtering pressure, Ar/

O_2 flow rate ratio, and RF power were fixed at 580 °C, 13 Pa, 9.5 sccm/0.5 sccm, and 30 W, respectively. For photovoltaic property measurements, 1 μm thick BFMO thin films were directly grown on vicinal STO substrates by an RF planar magnetron sputtering process. For BFMO growth, the substrate temperature, sputtering pressure, Ar/O_2 flow rate ratio, and RF power were fixed at 655 °C, 0.5 Pa, 3.5 sccm/1.5 sccm, and 50 W, respectively. Bi_2O_3, α-Fe_2O_3, and Mn_2O_3 powders were mixed and calcined with Bi/Fe/Mn composition ratios of $1.05/1-x/x$ ($x = 0$, 0.005, 0.01, 0.03 and 0.1), pressed into 4 inch diameter pellets and used as a target. For SXPES, SXAS, and HAXPES measurements, 150 nm thick BFMO thin films were grown on SRO-buffered vicinal STO substrates by an RF planar magnetron sputtering process with the conditions for BFMO growth described above. The BFMO thin films were also grown on dummy STO(001) substrates at the same lot for checking film thickness by cross-sectional SEM images. For measurement of the photovoltaic properties, 100×100 μm^2 Pt electrodes were deposited on the BFMO/STO surface by RF planar magnetron sputtering and a photolithography lift-off processes. For HAXPES measurements, 9 nm thick ultrathin Au films were deposited on the BFMO/SRO/STO surface by thermal evaporation.

SXPES and SXAS measurements. SXPES and SXAS measurements were performed at the BL-2A MUSASHI undulator beamline at the Photon Factory of The High Energy Accelerator Research Organization (KEK), Tsukuba, Japan. The SXAS spectra were recorded in total electron yield mode. The SXPES spectra were acquired using a VG-Scienta SES-2002 hemispherical analyzer. The SXPES and SXAS resolutions were set at approximately 100 and 80 meV, respectively.

HAXPES measurements. The HAXPES measurements were performed at the BL47XU at the SPring-8 synchrotron radiation facility, Sayo, Japan. Synchrotron radiation X-rays with an energy of 7.94 keV were used for photoelectron excitation. Bi 4f, Au 4f and valence band spectra were measured at RT and peak positions were corrected with respect to the Fermi edge of a gold film sample. The HAXPES spectra were obtained using the R4000 photoelectron analyzer (VG-Scienta Co.) equipped with a wide-acceptance-angle electrostatic lens with acceptance angle of about ± 32°[42,43]. Both the top Au-capped layer and SRO bottom electrodes were grounded simultaneously during the measurements.

Data availability

The datasets analyzed during the current study are available from the corresponding author on reasonable request.

Received: 18 June 2020; Accepted: 24 August 2020
Published online: 21 September 2020

References

1. Chynoweth, A. G. Surface space-charge layers in barium titanate. *Phys. Rev.* **102**, 705–714 (1956).
2. Koch, W. T. H., Munser, R., Ruppel, W. & Würfel, P. Bulk photovoltaic effect in $BaTiO_3$. *Solid State Commun.* **17**, 847–850 (1975).
3. Perterson, G. E., Glass, A. M. & Negran, T. J. Control of the susceptibility of lithium niobate to laser-induced refractive index changes. *Appl. Phys. Lett.* **19**, 130–132 (1971).
4. Glass, A. M., von der Linde, D. & Negran, T. J. Highvoltage bulk photovoltaic effect and the photorefractive process in $LiNbO_3$. *Appl. Phys. Lett.* **25**, 233–235 (1974).
5. Glass, A. M., von der Linde, D., Auston, D. H. & Negran, T. J. Excited state polarization, bulk photovoltaic effect and the photorefractive effect in electrically polarized media. *J. Electron. Mater.* **4**, 915–943 (1975).
6. Spanier, J. E. *et al.* Power conversion efficiency exceeding the Shockley-Queisser limit in a ferroelectric insulator. *Nat. Photonics* **10**, 611–614 (2016).
7. Poosanaas, P., Tonooka, K. & Uchino, K. Photostrictive actuators. *Mechatronics* **10**, 467–487 (2000).
8. Uchino, K., Aizawa, M. & Nomura, L. S. Photostrictive Effect in (Pb, La) $(Zr, Ti)O_3$. *Ferroelectrics* **64**, 199–208 (1985).
9. Nakashima, S., Hayashimoto, R., Fujisawa, H. & Shimizu, M. Bulk photovoltaic effects in Mn-doped $BiFeO_3$ thin films and the optical strains. *Jpn. J. Appl. Phys.* **57**, 11UF11-1–5 (2018).
10. Robertson, J., Warren, L. & Tuttle, B. Band states and shallow hole traps in Pb(Zr, Ti)O3 ferroelectrics. *J. Appl. Phys.* **77**, 3975–3980 (1995).
11. Ianculescu, A. *et al.* Optical characterization and microstructure of $BaTiO_3$ thin films obtained by RF-magnetron sputtering. *Appl. Sur. Sci.* **254**, 344–348 (2006).
12. Nastos, F. & Sipe, J. E. Optical rectification and shift currents in GaAs and GaP response: below and above the band gap. *Phys. Rev. B* **74**, 035201-1–15 (2006).
13. Young, S. M., Zheng, F. & Rappe, A. M. First-principles calculation of the bulk photovoltaic effect in Bismuth Ferrite. *Phys. Rev. Lett.* **109**, 2366015 (2012).
14. Bieler, M., Pierz, K., & Siegner, U. Simultaneous generation of shift and injection currents in (110)-grown GaAs/AlGaAs quantum wells. *J. Appl. Phys.* 100, 083710–1–7 (2006).
15. Tan, L. Z. *et al.* Shift current bulk photovoltaic effect in polar materials—hybrid and oxide perovskites and beyond. *Comput. Mater.* **2**, 16026-1–12 (2016).
16. Nakamura, M. *et al.* Shift current photovoltaic effect in a ferroelectric charge-transfer complex. *Nat. Commun.* **8**, 281-1–6 (2017).
17. Ogawa, N., Sotome, M., Kaneko, Y., Ogino, M. & Tokura, Y. Shift current in the ferroelectric semiconductor SbSI. *Phys. Rev. B* **96**, 24120314 (2017).
18. Wang, J. *et al.* Epitaxial $BiFeO_3$ multiferroic thin film heterostructures. *Science* **299**, 1719–1722 (2003).
19. Lebeugle, D. *et al.* Room-temperature coexistence of large electric polarization and magnetic order in $BiFeO_3$ single crystals. *Phys. Rev. B* **76**, 02411618 (2007).
20. Takahashi, K., Kida, N. & Tonouchi, M. Terahertz radiation by an ultrafast spontaneous polarization modulation of multiferroic $BiFeO_3$ thin films. *Phys. Rev. Lett.* **96**, 11740214 (2006).
21. Basu, S. R. *et al.* Photoconductivity in $BiFeO_3$ thin films. *Appl. Phys. Lett.* **92**, 091905-1–3 (2008).
22. Gu, J.-X. *et al.* Super-long-time relaxation of photo-induced influence on $BiFeO_3$ thin films. *J. Appl. Phys.* **118**, 204103-1–6 (2015).
23. Schick, D. *et al.* Localized excited charge carriers generate ultrafast inhomogeneous strain in the multiferroic $BiFeO_3$. *Phys. Rev. Lett.* **112**, 09760216 (2014).

24. Kundys, B., Viret, M., Colson, D. & Kundys, D. O. Light-induced size changes in $BiFeO_3$ crystals. *Nat. Mater.* **9**, 803–806 (2009).
25. Chu, Y.-H. *et al.* Domain control in multiferroic $BiFeO_3$ through substrate vicinality. *Adv. Mater.* **19**, 2662–2666 (2007).
26. Jang, H. W. *et al.* Domain engineering for enhanced ferroelectric properties of epitaxial (001) $BiFeO_3$ thin films. *Adv. Mater.* **21**, 81–8237 (2009).
27. Nakashima, S. *et al.* Structural and ferroelectric properties of domain-structure-controlled $BiFeO_3$ thin films prepared by dual-ion-beam sputtering. *Jpn. J. Appl. Phys.* **51**, 09LB02-1–5 (2012).
28. Nakashima, S. *et al.* Influence of lattice distortion induced by a vicinal $SrTiO_3$(001) substrate in single-domain $BiFeO_3$ Thin films prepared by radio frequency planar magnetron sputtering. *Jpn. J. Appl. Phys.* **52**, 090317 (2013).
29. Ji, W., Yao, K. & Liang, Y. C. Evidence of bulk photovoltaic effect and large tensor coefficient in ferroelectric $BiFeO_3$ thin films. *Phys. Rev. B* **84**, 09411515 (2011).
30. Nakashima, S. *et al.* Bulk photovoltaic effect in a $BiFeO_3$ thin film on a $SrTiO_3$ substrate. *Jpn. J. Appl. Phys.* **53**, 09PA16-1–4 (2014).
31. Nakashima, S., Takayama, T., Uchida, T., Fujisawa, H. & Shimizu, M. Anomalous photovoltaic effects in Pt/single-domain-structured $BiFeO_3$/Pt coplanar capacitors on $SrTiO_3$ substrates. *Jpn. J. Appl. Phys.* **54**, 10NA16-1–6 (2015).
32. Nakashima, S., Takayama, K., Shigematsu, K., Fujisawa, H. & Shimizu, M. Growth of epitaxial Mn and Zn codoped $BiFeO_3$ thin films and an enhancement of photovoltage generated by a bulk photovoltaic effect. *Jpn. J. Appl. Phys.* **55**, 10TA07-1–5 (2016).
33. Nakashima, S. *et al.* Strain evolution of epitaxial tetragonal-like $BiFeO_3$ thin films on $LaAlO_3$(001) substrates prepared by sputtering and their bulk photovoltaic effect. *Jpn. J. Appl. Phys.* **55**, 101501-1–9 (2016).
34. Matsuo, H., Noguchi, Y. & Miyayama, M. Gap-state engineering of visible-light-active ferroelectrics for photovoltaic applications. *Nat. Commun.* **8**, 207-1–8 (2017).
35. Bhatnagar, A., Chaudhuri, A. R., Kim, Y. H., Hesse, D. & Alexe, M. Role of domain walls in the abnormal photovoltaic effect in BiFeO3. *Nat. Commun.* **4**, 283518 (2013).
36. Ederer, C. & Spaldin, N. A. Effect of epitaxial strain on the spontaneous polarization of thin film ferroelectrics. *Phys. Rev. Lett.* **95**, 25760114 (2005).
37. Sando, D. *et al.* Revisiting the optical band gap in epitaxial $BiFeO_3$ thin films. *Adv. Opt. Mater.* **6**, 170083618 (2018).
38. Naganuma, H., Miura, J. & Okamura, S. Ferroelectric, electrical and magnetic properties of Cr, Mn Co, Ni, Cu added polycrystalline BiFeO3 films. *Appl. Phys. Lett.* **93**, 05290113 (2008).
39. Zhong, Z., Singh, S. K., Maruyama, K. & Ishiwara, H. Comparative studies on ferroelectric properties of Mn-substituted $BiFeO_3$ thin films deposited on Ir and Pt electrodes. *Jpn. J. Appl. Phys.* **47**, 2230–2233 (2008).
40. Singh, S. K., Ishiwara, H., Sato, K. & Maruyama, K. Microstructure and frequency dependent electrical properties of Mn-substituted $BiFeO_3$ thin films. *J. Appl. Phys.* **102**, 09410915 (2007).
41. Noguchi, Y., Matsuo, H., Kitanaka, Y. & Miyayama, M. Ferroelectrics with a controlled oxygen-vacancy distribution by design. *Sci. Rep.* **9**, 4225110 (2019).
42. Ikenaga, E. *et al.* Development of high lateral and wide angle resolved hard X-ray photoemission spectroscopy at BL47XU in SPring-8. *J. Electron Spectrosc. Relat. Phenom.* **190**, 180–187 (2013).
43. Ikenaga, E. *et al.* Hard X-ray photoemission spectroscopy at two public beamlines of SPring-8: current status and ongoing developments. *Sync. Rad. News* **31**, 10–15 (2018).

Acknowledgements

This research is supported in part by KAKENHI Grants-in-Aid (Nos. JP19K04495 and JP16K06272) from the Japan Society for the Promotion of Science (JSPS). The HAXPES experiments reported herein were performed under the approval of the Japan Synchrotron Radiation Research Institute (JASRI)/SPring-8 (Proposal No. 2017A1430). The SXPES and SXAS experiments reported herein were performed under the approval of The High Energy Accelerator Research Organization/Photon Factory (KEK/PF) (Proposal No. 2018G003). The authors would thank to Mr. K. Takayama and Mr. K. Shigematsu for helping sample preparation and photovoltaic properties measurements.

Author contributions

S.N., H.F., T.K., T. H. and M.S. conceived and designed the experiments. S.N. and M.S. contributed to sample preparation and photovoltaic properties measurements, H.F. and S.N. conducted XRD, PFM, and D-E hysteresis measurements. S.N., H.F. A.Y. and T.K. performed HAXPES measurements. S.N., T.H. conducted SXPES and SXAS measurements. S.N. H.F., T.H. and A.Y. co-wrote this paper.

Competing interests

The authors declare no competing interests.

Additional information

Supplementary information is available for this paper at https://doi.org/10.1038/s41598-020-71928-5.

Correspondence and requests for materials should be addressed to S.N.

Reprints and permissions information is available at www.nature.com/reprints.

Publisher's note Springer Nature remains neutral with regard to jurisdictional claims in published maps and institutional affiliations.